Comparative in Operando Studies in Heterogeneous Catalysis: Atomic and Electronic Structural Features in the Hydrogenation of Ethylene over Supported Pd and Pt Catalysts

Ulrich Jung,[†] Annika Elsen,[†] Yuanyuan Li,[‡] Jeremy G. Smith,[†] Matthew W. Small,[†] Eric A. Stach,[#] Anatoly I. Frenkel,*[‡] and Ralph G. Nuzzo*[†]

[†]Department of Chemistry, University of Illinois, Urbana, Illinois 61801, United States
[‡]Department of Physics, Yeshiva University, New York, New York 10016, United States
[#]Center for Functional Nanomaterials, Brookhaven National Laboratory, Upton, New York 11973, United States

S *Supporting Information*

ABSTRACT: There exists an emerging opportunity, engendered by advances made in experimental methods of research, to address long-standing questions about the nature of the molecular mechanisms that are operative in important heterogeneous catalytic processes, as well as the nature of the complex atomic and electronic structural features that mediate them. Of particular interest in this regard is the understanding of the dynamical attributes of catalytic processes—an understanding that might allow design principles to be applied to optimize the atomic and electronic structure of heterogeneous catalysts to sustain their performance in essentially any operating process condition. The current work explores these ideas—highlighting capabilities of in operando methods of spectroscopic characterization as applied to

Catalyst Structural Evolution During Ethylene Hydrogenation

an exemplary heterogeneous catalytic process, olefin hydrogenation. No heterogeneous catalytic process has been studied more intensively than olefin hydrogenation. The extensive literature available establishes important features by which metal catalysts activate and efficiently transform the bonding of the hydrogen and alkene reactants to generate a product alkane. Even so, many important mechanistic questions remain poorly understood due to the inherent multiscale complexity associated with heterogeneous catalytic transformations, as well as the paucity of methods suitable for their characterization in operando. The recent literature documents the development of new capabilities for characterization afforded by in situ and in operando methods. Of these, X-ray absorption spectroscopy (XAS) has become a particularly important technique for studying the mechanisms of catalytic reactions due to its capabilities for elucidating the nature of the atomic and electronic structural features of operating catalysts. Many important questions can now be addressed, in particular those that follow from the unique dynamical impacts and patterns of reactivity that occur in higher pressure (non-UHV) environments. In this Perspective, we examine important structure–property correlations for an exemplary model reaction—ethylene hydrogenation—as elucidated in operando for two efficient catalyst materials—nanoscale Pd and Pt clusters supported on SiO₂. The examined features include the following: the structural dynamics of the metal clusters and their sensitivity to the composition of the reactant feed; the role of hydrogen, and metal- and/or support-bonded forms of adsorbates more generally, in forming intermediates and products; the influences of adsorbate bonding states (e.g., hydrogen) on reactivity; the role played by carbonaceous deposits (and the mechanisms of their formation); the quantitative nature of the atomistic features that exist within the structure–sensitivity correlations of this catalytic reaction; and mechanisms that mediate the sintering of catalysts operating in high-pressure ambient environment. Here we present a comparative overview of the hydrogenation of ethylene over ≈1 nm-sized Pd and Pt catalysts supported on SiO₂. The reaction was characterized in various mixed hydrogen and ethylene atmospheres at ambient conditions by in operando XAS and complemented with scanning transmission electron microscopy (STEM). Pronounced changes in the atomic and electronic structures of both catalysts (e.g., defined transitions between hydrogen- and hydrocarbon-covered surfaces, carbide-phase formation, hydrogen (de)intercalation, and particle coarsening) are found to occur during the reaction. The evolution of the catalysts features, however, has only minimal impact on the largely reversible patterns of reactivity. These findings demonstrate remarkable dynamic structural complexity within the mechanisms of alkane formation over both types of supported catalysts.

KEYWORDS: *supported metal nanocatalysts, ethylene hydrogenation, X-ray absorption spectroscopy (XAS), in operando study, atomic structure, structural dynamics, scanning transmission electron microscopy (STEM)*
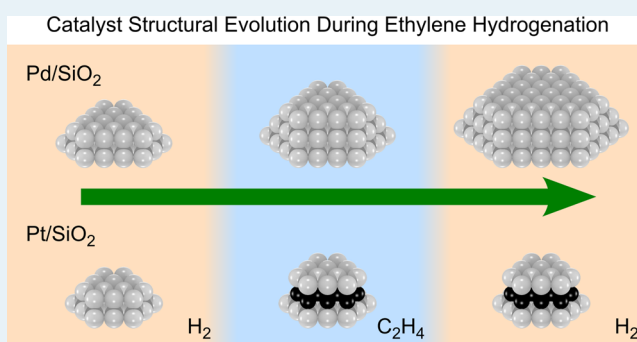
■ INTRODUCTION

Supported metal catalysts are widely used in industrial applications because they exhibit high structural flexibility and stability and their reactivity and selectivity can be precisely controlled.[1−3] These systems, however, are only poorly characterized in terms of the dynamic structural properties that determine their overall performance.[1−3] It is therefore important to improve both the understanding of the processes that occur on the atomic/molecular level as well as the parameters that control reactivity and selectivity (so-called catalytic descriptors). This is mainly done by employing well-defined model systems.[1,3,4] The most important are single crystals, studied under ultrahigh vacuum (UHV) conditions,[1,3,4] and supported catalysts, prepared from high-purity materials, with well-defined structures and sizes, studied under reaction conditions.[1−4] There are numerous examples of apparent discrepancies between these model systems, which have been attributed to differences in the samples or experimental conditions (the so-called material and pressure gap).[5−7] Much work has focused on overcoming these differences and providing predictive understanding of catalyst structure/property/rate correlations over diverse ranges of experimental conditions, especially those more closely approximating the high pressure/temperature operating regimes of industrial catalysis (where pressures reaching to several hundred bars and temperatures far above ambient are common).[6,7]

The present study addresses the atomic and electronic structural dynamics evidenced by supported nanoparticles during the catalytic hydrogenation of ethylene at atmospheric pressure, adding insights that are both complex and underappreciated in the current literature. Such effects have been in the focus of a rapidly growing number of investigations in the past decade and are likely to affect the understanding of heterogeneous catalysis and the mechanisms that mediate catalytic formation/transformation of C−H bonds over supported metal clusters. A brief overview of the literature is provided, framing a context for considering the surprising structural dynamics exhibited by Pd and Pt catalysts supported on SiO$_2$ during the hydrogenation of ethylene.

The hydrogenation of unsaturated hydrocarbons over transition metals is perhaps the longest known (initial work was carried out by Paul Sabatier in 1893)[8] and most-intensively studied class of catalytic reaction, in part because of its considerable economic importance in diversified chemical (e.g., fat hardening) and oil industries (conversion of unsaturated hydrocarbons to paraffins and naphthenes, hydrocracking).[3,9,10] Because ethylene is the simplest unsaturated hydrocarbon, it has been widely used as a model compound.[11] Comparatively fewer works have employed higher alkenes (mainly propylene to hexenes)[12−14] or alkynes (e.g., acetylene).[13,15−17] This engenders problems for developing a broader understanding of more complex industrial processes, because the reactivity of ethylene differs considerably from that of its higher homologues (e.g., higher alkenes can exhibit cis−trans isomerism[14] and double-bond migration[18,19]).

The hydrogenation of ethylene has been studied using many different physical forms of materials as catalysts (e.g., single crystals, thin films, wires, powders, and supported nanoparticles of most group 8 to 10 metals) and under a diverse range of experimental conditions of both temperature and pressure.[20−22] In particular, supported particles have been extensively employed (e.g., Ni/SiO$_2$,[23] Ru/Al$_2$O$_3$,[24] Rh/Al$_2$O$_3$,[24] Pd/Al$_2$O$_3$,[15,24−26] Pd/SiO$_2$,[27,28] Ir/Al$_2$O$_3$,[12] Pt/MgO,[29] Pt/Al$_2$O$_3$,[12,24,29−33] Pt/SiO$_2$,[23,29,34−40] Pt/(Al$_2$O$_3$, SiO$_2$),[29] and Pt/TiO$_2$[29]).

Very similar reaction orders of hydrogen and ethylene, rates, and activation energies have been reported for these systems.[20−22,34,38,41−43] For steady-state conditions, where the conversion is not mass-transfer limited, the reaction order of hydrogen changes from ≈0.5 at lower temperatures to ≈1 at room temperature and above and that of ethylene from ≈ −1 at pressures below 75 Torr to ≈0 above that point.[38,43] The hydrogenation rates are typically very high, even at room temperature, with turnover frequencies of 1−100 monolayers (ML) per second.[20,21,44,45] They seem to be unaffected by the surface morphology of the catalyst; that is, the reaction is apparently structure-insensitive. This means that, as classically defined, the reactivity changes very little as the dispersion of a supported catalyst is varied, other than as a consequence of a difference in its effective surface area.[20−22] The activation energies, as might be expected intuitively for such cases, vary weakly—typically ranging between 35−45 kJ mol^{-1}.[20−22,34,38,41−43]

The pressure- and temperature-dependent changes in reaction order can be explained in terms of the nature of the competitive adsorption of hydrogen and ethylene (i.e., by a transition from a less competitive adsorption reaction pathway at lower pressures and temperatures to a more competitive at higher pressures and temperatures).[38,43] The adsorption of ethylene on metal surfaces is very complex, and evidence a pronounced temperature dependence (this is addressed in more detail in the Supporting Information). At lower temperatures, ethylene adsorbs on Pt either as a weakly bound π complex or via the formation of two σ bonds (di-σ species).[46] The latter species can dehydrogenate at higher temperatures to ethylidyne,[42,47,48] a reaction likely proceeding through an ethylidene intermediate.[49] Di-σ ethylene and ethylidyne compete for binding sites, whereas π ethylene does not.[50,51] At room temperature, most ethylidyne and less di-σ and π ethylene were found to coexist on Pd/SiO$_2$ (4.3 wt %, size <5 nm),[27] whereas only ethylidyne was identified on Pt/SiO$_2$ (5.6 wt %, size 2−5 nm).[40] It is reported that the hydrogenation steps proceed at a much higher rate for π ethylene than for di-σ ethylene (by ≈2−3 orders of magnitude)[44] and for the latter species at a much higher rate than for ethylidyne (by ≈2 orders of magnitude).[44] These data have been interpreted to suggest that the activity for alkane formation does not follow directly from the surface coverage of either ethylidyne or di-σ ethylene, but only from that of the π ethylene.[50,51]

When taken together, the broad literature supports a reaction mechanism originally proposed by Horiuti and Polanyi in 1934,[52] that is, the stepwise incorporation of two surface-adsorbed hydrogen atoms by a surface-adsorbed ethylene molecule via an ethyl intermediate.[23,33] The first hydrogenation step, converting π ethylene to a surface-bound ethyl intermediate, is generally accepted to be rate-determining, the ethyl coverage is very low under all conditions studied.[23,33] Other possible intermediates such as vinylidene, vinyl, or ethylidene have not been identified in surface science experiments and likely do not play an important mechanistic role in this reaction.[49] The second hydrogenation step, converting the ethyl intermediate to ethane, a formal reductive elimination of the ethyl group with adsorbed hydrogen, competes (generally) unfavorably with a reverse β-hydride elimination to ethylene,[53,54] as has been demonstrated by isotope exchange experiments (i.e., hydrogenation experiments with ethylene and deuterium),[11,13,22,43,55,56] in which essentially all possible deuterated ethane isotopomers were obtained. A ^{14}C labeling experiment clearly showed that the C−C bond is stable during the reaction.[57] Ethane adsorbs only

very weakly and thus is not expected to affect the overall reactivity significantly.

Pd, unlike most other high-activity metal catalysts such as Pt, can reversibly incorporate hydrogen and form hydrides.[58] At atmospheric pressure and room temperature, two phases of palladium hydride are known to exist, α- and β-PdH$_n$[58] (additional details are given in the Supporting Information). There is evidence that in some cases steps of the ethylene hydrogenation may involve both subsurface and surface-bound forms of hydrogen.[59]

It is clear that all these aspects do not fully explain important, and what remain as challenging, experimental features of the overall mechanism of reactivity (e.g., the reaction orders, the apparent structure insensitivity, the in operando nature and dynamics of the metal−metal (M−M) and metal−adsorbate (M−ads) bonding present in small metal cluster catalysts). This emphasizes the relevance of the complex coupling of elementary reactions and the mediation of the main reactions by a rich surface chemistry of intermediate/transient adsorbate species (e.g., due to surface exchange reactions, the dehydrogenation of ethylene to ethylidyne, and, in the case of Pd, the intercalation/deintercalation of hydrogen). Their evolution and, perhaps most importantly, the transformations of the structure of the metal catalysts themselves as used in supported high-dispersion (nanoscale) forms remain incompletely understood.

Pd and Pt nanoparticles on C, SiO$_2$, and γ-Al$_2$O$_3$ supports have been intensively studied by X-ray absorption spectroscopy (XAS), because this method yields extensive information about their geometric structure and electronic properties.[60,61] The X-ray absorption near-edge structure (XANES) is sensitive to electronic properties (e.g., the absorption edge energy depends on the unoccupied density of states near the Fermi energy[60,61]) and the extended X-ray absorption fine structure (EXAFS) gives detailed structural information (e.g., coordination numbers, interatomic distances, and Debye−Waller factors[60,61]). It has become common to perform XAS experiments under reaction conditions.[62] The work on supported Pd particles[63−69] has mainly focused on changes in structural order upon hydrogen exposure. Compared to fully metallic clusters, which are present in inert atmospheres, the particles in hydrogen atmospheres exhibited significantly reduced structural order and increased lattice constants, indicative of the formation of a palladium hydride phase.[69] Moreover, the amount of incorporated hydrogen and the ratio of bulk-to-surface-adsorbed hydrogen were found to increase with increasing particle size.[69] In contrast, for Pd/Al$_2$O$_3$ in ethylene atmospheres identical structural parameters were identified as in inert atmospheres.[64,65] No significant support effects were found for such particles, with the exception of the formation of a carbide phase for Pd/C.[64,65] For supported Pt particles upon adsorption of hydrogen a relaxation of the Pt−Pt bonds was identified.[70] In addition, a XANES peak due to Pt−H bonding was observed, which can be used to monitor the hydrogen coverage variously present during catalytic reactions.[70] For both Pt/SiO$_2$[71] and Pt/Al$_2$O$_3$,[72] pronounced structural differences were found to exist between hydrogen and ethylene atmospheres.

Here, the hydrogenation of ethylene, a highly exemplary reaction, is revisited, illustrating new insights that emerge from comparative in operando XAS and mass spectroscopy (residual gas analysis, RGA) studies of ethylene hydrogenation over nanoscale (~1−2 nm) Pd and Pt catalysts supported on SiO$_2$. These data come from measurements made in various atmospheres of mixed compositions ranging from pure hydrogen to ethylene at ≈1 atm total pressure and ambient temperature and are complemented with scanning transmission electron microscopy (STEM) studies of the pristine catalysts and those recovered after the in operando experiments. The results reveal that the reaction embeds significant forms of dynamic structural complexity, e.g., transitions between hydrogen- and hydrocarbon-covered surfaces, carbide-phase formation, hydrogen (de)intercalation, and particle coarsening, among others that attend to the efficient conversion of ethylene to ethane. The simple mass-transfer controlled reactivity of these systems masks what is otherwise a remarkable form of complexity in the atomic and, by inference, electronic structure of the metal nanoparticle catalysts. The trends that emerge define a challenging set of benchmarks that experiment and theory might in time come to address.

■ EXPERIMENTAL SECTION

Nanoparticle Synthesis. The Pd and Pt nanoparticle catalysts were prepared by wet impregnation onto the SiO$_2$ support and subsequent reduction in hydrogen. The nominal weight loading was 1%. A detailed description of the synthesis is given in the Supporting Information.

Scanning Transmission Electron Microscopy. To determine the size distributions of the supported catalyst particles, high-angle annular dark-field scanning transmission electron microscopy (HAADF-STEM) measurements were carried out using a JEOL 2010F EF-FEG STEM (JEOL, Ltd.). The details about the experimental setup, STEM samples, and the partially automated particle size analysis routine are provided in the Supporting Information.

X-ray Absorption Spectroscopy. *Experimental Details.* The XAS experiments were performed at the beamlines X18B (Pd K-edge) and X19A (Pt L$_3$-edge) at the National Synchrotron Light Source at Brookhaven National Laboratory. Further information about the beamline setups is given in the Supporting Information.

The supported catalysts were studied during catalytic reaction using a Clausen plug-flow reaction cell,[73] consisting of a Kapton tube with an inner diameter of 3 mm and providing uniform access of the reaction gas mixture to the catalyst powder. The horizontal size of the X-ray beam probing the catalyst powder in the cell was selected to be smaller than the length of the packed powder, to maximize the X-ray data quality. At these dimensions, and for the gas flows used, the conversions of the reactant gases (ethylene and hydrogen) were generally mass-transfer limited, affording a yield of ethane determined by the limiting gas concentration present in the reactor feed. It should be noted that the high conversion efficiencies so engendered will lead to gradient profiles of reactivity within the reactor that will be composition-dependent. The XAS data presented below are not able to spatially resolve a gradient structural profile generated in the catalyst bed as the gas composition is varied. This feature, however, does not impact the nature or analyses of structure made where the feeds reach limiting values of composition (hydrogen- or ethylene-rich, as are discussed below) during forward and reverse cycling. The cell was purged with mixtures of hydrogen (99.999% purity) and ethylene (99.9% purity) of variable compositions. Specifically, the gas composition was varied from pure hydrogen to ethylene in the following sequence (giving only the relative hydrogen content Q_{H_2}): 100.0, 80.0, 60.0, 55.0, 52.5, 50.0, 47.5, 45.0, 42.5, 40.0, 35.0, 30.0, 25.0, 20.0, 10.0, and 0.0%. Afterward, it was altered in the reverse sequence from pure ethylene to hydrogen. The gas compositions and flow
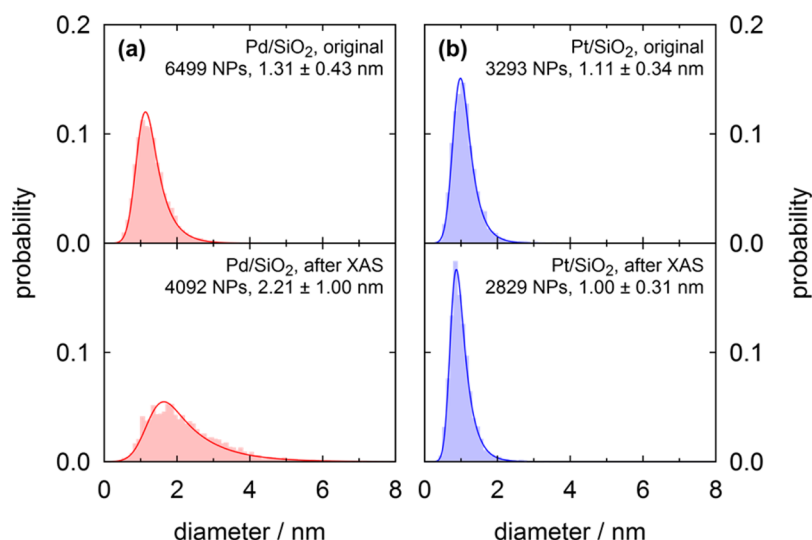
Figure 1. Size distributions obtained from the STEM measurements of (a) Pd/SiO_2 and (b) Pt/SiO_2 used in the XAS experiments.

rates were controlled using mass-flow controllers (Brooks Model 5850E). The flow rate was held constant at 20 mL min^{-1} throughout the whole measurement sequence. The pressure in the flow cell was slightly above atmospheric pressure. The composition of the exhaust gases was analyzed with a residual gas analyzer (RGA 200, Stanford Research Systems, Inc.). Due to the different, nonlinear responses of the RGA setups at the two beamlines, the pressures were calibrated before determination of the ethane conversion yields. The procedure is described in the Supporting Information. All measurements were carried out under steady-state conditions, typically reached after ≥ 30 min, at room temperature. For each gas composition, three spectra were measured, which took ≈3 × 15 min.

Data Analysis. XAS data analysis was performed using the IFEFFIT software package (version 1.2.11c).[74] The spectra were preprocessed with the Athena software (version 0.8.061),[75] as described in the Supporting Information, and then fitted with the Artemis software (version 0.8.014).[75] The photoelectron scattering amplitudes and phases for the model structures of bulk Pd, Pt, and α-PtO_2 were calculated with FEFF6.[74] The k^2-weighted EXAFS spectra $\chi(k)$ were Fourier-transformed to yield the radial structure functions $\chi(r)$, which were used for fitting.

The Pd/SiO_2 fitting model comprised only the first Pd−Pd scattering path. The energy shift ΔE_0 was constant for all spectra, whereas the degeneracy of the scattering path (i.e., coordination number) n, effective half-path length (i.e., bond distance) r, and mean-square deviation (i.e., Debye−Waller factor) σ^2 were variable for each spectrum. The constant energy shift was obtained as weighted average from the results of an analogous fitting model with variable energy shifts. Fitting was performed in the r-range of 1.675−3.475 Å and the k-range of 2.5−15 Å^{-1}. The model uses 108 parameters to account for 508 data points. A Pd-low-Z contribution at ≈2 Å, probably less pronounced in the hydrogen-rich than in the ethylene-rich atmospheres, could not be incorporated into a consistent fitting model, because it was too small to quantify.

For Pt/SiO_2 a more complex fitting model was required: The spectra measured in the initial hydrogen-rich atmospheres could be described considering only the first Pt−Pt scattering path. For the spectra measured in the ethylene-rich atmospheres, in addition two paths between Pt and their low-Z neighbors,

modeled as Pt−O paths with assigned initial shifts from the model distance (by ≈ + 0.2 Å and ≈ − 0.2 Å, respectively), to account for the so-called long and short bond, were necessary. These shifts were later refined in the final fits, and the distances of the Pt-LB and Pt-SB (with LB: long bond and SB: short bond) were obtained. For the spectra measured in the final hydrogen-rich atmospheres, aside from the Pt−Pt path, only the long-bond Pt-low-Z path was needed. The energy shift ΔE_0 was constant for all spectra and scattering paths. The coordination numbers n_{Pt-Pt}, n_{Pt-LB}, n_{Pt-SB} of the different scattering paths were constant for the spectra measured in the initial hydrogen-rich atmospheres, the ethylene-rich atmospheres, and the final hydrogen-rich atmospheres, respectively. All other parameters, namely, the bond distances r, the Debye−Waller factors σ^2, and the third cumulants of the Pt−Pt path $\sigma_{Pt-Pt}^{(3)}$ were variable. The constant energy shift and coordination numbers were obtained as weighted averages from the results of an analogous fitting model with variable energy shifts and coordination numbers. Fitting was performed in the r-range of 1.4−3.25 Å or 1.7−3.25 Å for the spectra measured in the initial hydrogen-rich and ethylene-rich atmospheres or final hydrogen-rich atmospheres, respectively, and the k-range of 3−15 Å^{-1} or 3−13.5 Å^{-1} for those in the hydrogen- or ethylene-rich atmospheres, respectively. The model uses 201 parameters to account for 444 data points. In addition, a model with variable coordination numbers, analogous to that for Pd/SiO_2, was tested. Because no significant variations in the coordination numbers were identified within the initial hydrogen-rich, ethylene-rich, and final hydrogen-rich atmospheres, respectively, and the fitting quality was very similar, constraining the coordination numbers was justified.

RESULTS AND DISCUSSION

Catalyst Particle Size Distributions. Representative STEM images of the supported metal catalysts are shown in the Supporting Information (Figure S1). For both the pristine Pd/SiO_2 and Pt/SiO_2 particles, well-defined and narrow size distributions are obtained (Figure 1a,b, top). The average particle sizes are 1.31 ± 0.43 nm (6499 particles) and 1.11 ± 0.34 nm (3293 particles), respectively. After the in operando XAS experiment, the Pd/SiO_2 particles exhibit a much broader distribution (Figure 1a, bottom) with a considerably increased average size of 2.21 ± 1.00 nm (4092 particles), revealing that

they experienced pronounced agglomeration. In contrast, for the Pt/SiO$_2$ particles (Figure 1b, bottom) the cluster sizes in the recovered catalyst have a size distribution of 1.00 ± 0.31 nm (2829 particles), a value unchanged within the limits of experimental uncertainty; that is, the average particle structure is not significantly altered during the XAS experiment. This is also supported by the fact that no Z-contrast differences are evidenced in the STEM images of the pristine Pt catalyst particles and that after the XAS experiment. The importance of these results is discussed in detail in the sections that follow.

Composition-Dependent Ethane Conversion over the Supported Catalysts. The steady-state ethane yields (the normalized fraction of the ethylene converted) obtained over the supported catalysts as a function of the reactant gas composition (flowing mixtures of ethylene and hydrogen at 1 atm total pressure) were measured during the XAS experiments via an in-line RGA analysis of the reactor effluent, and these data are shown in Figures 2a,b (see also the Supporting Information and
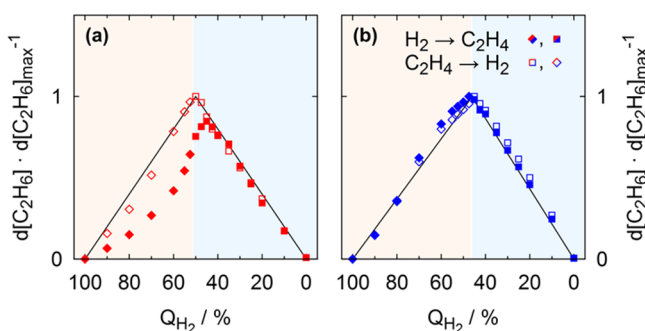

Figure 2. Normalized corrected steady-state C$_2$H$_6$ yields obtained in different mixtures of H$_2$ and C$_2$H$_4$ over (a) Pd/SiO$_2$ and (b) Pt/SiO$_2$ measured by in-line mass spectroscopy (residual gas analysis, RGA) during the XAS experiments. For details about the data analysis, refer to the text as well as the Supporting Information. The gas composition was gradually changed from pure H$_2$ to C$_2$H$_4$ and back again to H$_2$. Filled symbols indicate the forward sequence from H$_2$ to C$_2$H$_4$, and open symbols depict the backward sequence from C$_2$H$_4$ to H$_2$; diamonds are H$_2$-rich gas mixtures, and squares are C$_2$H$_4$-rich gas mixtures.

Figure S2). Within the sequence of measurements (from pure hydrogen to ethylene and back to hydrogen), the ethane yields increase in the hydrogen-rich atmospheres and similarly decrease in the ethylene-rich atmospheres. These trends vary approximately linearly with a pronounced maximum at intermediate gas compositions (i.e., at ≈50% hydrogen content). For Pd/SiO$_2$, initially in the forward sequence from pure hydrogen to ethylene, the yields deviate from that for Pt/SiO$_2$ (i.e., they initially are systematically smaller and increase nonlinearly, a feature that probably reflects some degree of adventitious poisoning of the as prepared catalyst). Additional control experiments, in which the catalysts were pretreated by oxidization and reduction at 200 °C for 1 h each, strongly support this interpretation; carbide phase formation can be excluded on the basis of the results of the EXAFS fitting presented below. The overall linear variations in the ethane yields demonstrate that in the hydrogen-rich atmospheres virtually all ethylene is consumed, and in the ethylene-rich atmospheres all hydrogen is consumed—indicating that the reactivity depends directly on the contents of the minority species in the feed gas (cf. Supporting Information) and thus is not significantly affected by changes in the catalyst's state. The important consequence that results from the operation of the catalysts under conditions *where the conversions are mass-transfer*

limited in this way is that they lead to a steady-state ambient that strongly weights hydrogen-dominated catalyst surface interactions in the one limiting conversion regime and hydrocarbon-derived ones in the other (a simplifying feature from the perspective of the EXAFS studies described below).

Some inferences can be made about the nature of the power-rate dependences that would characterize operation of these catalysts using a plug-flow reactor sized and operated to explicitly enable their direct measurement. The literature in this regard suggests generally simple kinetics that proceed with an overall first-order rate dependence on the hydrogen content and a zero-order dependence on the ethylene content over a major range of the experimental conditions examined here.[20−22,34,38,41−43]

Electronic Properties of the Catalysts Measured in Operando. The XAS spectra of the Pd/SiO$_2$ and Pt/SiO$_2$ catalysts as measured in pure hydrogen and ethylene atmospheres, respectively, are shown in Figure 3 and the Supporting
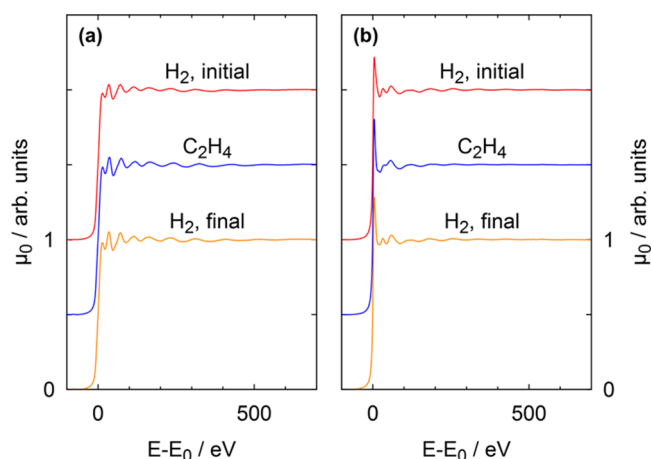
Figure 3. (a) Step-edge normalized XAS spectra of the K-edge (E_0 = 24 353.5 eV) for Pd/SiO$_2$ in pure H$_2$ and C$_2$H$_4$, respectively. (b) Analog spectra of the L$_3$-edge (E_0 = 11 563.7 eV) for Pt/SiO$_2$. All measurements were carried out under steady-state conditions.

Information (Figure S3). Difference XAS spectra of the whole measurement sequence from pure hydrogen to ethylene and back to hydrogen with respect to the initial measurement in hydrogen are given in Figure 4 and the Supporting Information (Figures S4−S6).

In the K-edge XANES spectra of Pd/SiO$_2$ in the various mixed atmospheres, only relatively small differences can be identified (Figures 3a and 4a; the Supporting Information: Figures S3, S4, and S6). In the initial forward sequence from pure hydrogen to ethylene in the hydrogen-rich atmospheres, the XAS oscillations gradually shift by a few eV to higher energies, and their amplitudes increase. A pronounced transition occurs between mixed atmospheres of 52.5 and 50.0% hydrogen content (i.e., at the point of the maximum ethane yield). In the ethylene-rich atmospheres, relatively small changes are exhibited. In the backward sequence from pure ethylene to hydrogen, a transition is evidenced, again at the same gas composition at which a similar structural transition was seen in the forward sequence. Upon returning to the hydrogen-rich atmospheres, the XAS oscillations gradually shift back to lower energies, and their amplitudes decrease, albeit with some evident irreversibility. This difference is correlated with an increase of conversion of ethylene to ethane, as noted in the section above.
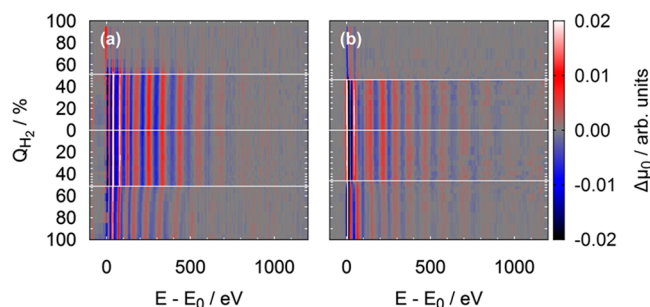
Figure 4. Difference normalized XAS spectra for (a) Pd/SiO$_2$ and (b) Pt/SiO$_2$ with respect to the initial spectrum in pure H$_2$. During each measurement, the sample was purged with mixtures of H$_2$ and C$_2$H$_4$ of different compositions. The composition was gradually changed from H$_2$ to C$_2$H$_4$ and back again to H$_2$. The total flow rate was 20 mL min^{-1}. All measurements were carried out under steady-state conditions. The measurement sequence is shown from top to bottom. Each spectrum is indicated by a mark.

Because the Pd K edge arises due to electronic transitions occurring between 1s states and unoccupied 5p$_{1/2}$ and 5p$_{3/2}$ states, it is not possible to obtain direct information from the XANES spectra about the electronic structure of the supported Pd particles, but instead, only less direct information about their geometrical properties and impacts due to support- and adsorbate-related bonding can be obtained. The XANES spectra measured in the hydrogen- and ethylene-rich atmospheres agree very well with the findings of an earlier study of 3.5 nm Pd particles supported on Al$_2$O$_3$,[64] which associated the spectroscopic changes with pronounced structural transformations that most probably arise due to changes in the adsorbate bonding states. In the hydrogen-rich atmospheres, multiple bound forms of hydrogen are most prevalent on (and within, see below) the Pd particles, whereas in the ethylene-rich atmospheres, the habits are dominated by the coverage of ethylene-derived, carbonaceous species (mainly ethylidyne). Still, to quantitatively account for the precise features in these data, additional forms of gross structural transformation are required, notably that there might occur a coarsening due to adsorbate-mediated particle growth. This point is discussed in more detail below.

In the L$_3$-edge XANES spectra of Pt/SiO$_2$ measured in the initial hydrogen-rich atmospheres (Figure 3b and 4b; Supporting Information Figures S3, S5, and S6), the peak closest to the absorption edge (the so-called white line) is quite broad and asymmetric, clearly exhibiting a shoulder at higher energies. This line shape does not change significantly, but the intensity decreases continuously as the gas composition nears the region at which the maximum ethane yield is obtained. Analogously to Pd/SiO$_2$, a pronounced transition occurs at mixed composition atmospheres near 50% hydrogen content. In contrast, however, the transition in this case is more abrupt. The white line becomes narrower and more symmetric, and its intensity increases considerably. In addition, a small peak appears at 19 eV, and the peak at 32 eV shifts by ≈5 eV to higher energies. The EXAFS oscillations also shift to higher energies, and their amplitudes decrease. Within the ethylene-rich atmospheres, the variations evidenced are only minor. In the backward sequence, a transition occurs at the same gas composition as found in a correlated form in the forward sequence. An important form of hysteresis is noted here, though, namely, that the white line changes only slightly, maintaining characteristics similar as were found in the ethylene-rich atmospheres (i.e., narrower and more intense than in the

initial hydrogen-rich atmospheres). Most importantly, the peak at 19 eV is retained. The EXAFS oscillations largely recover, albeit with smaller amplitudes. The transformations of both atomic and electronic structure are thus not fully reversible, indicating an underlying change in the Pt catalyst's structure and/or composition has occurred. The results of the EXAFS fitting discussed below show that retained carbonaceous species are responsible for these impacts.

The Pt L$_3$ edge originates from transitions from the 2p$_{3/2}$ states to unoccupied 5d$_{3/2}$, 5d$_{5/2}$, and 6s states, with a dominant contribution of the 5d$_{5/2}$ states (e.g., by a factor of 14 larger than that of the 5d$_{3/2}$ states).[76,77] Because the unoccupied states near the Fermi energy are mainly of 5d character, the absorption edge and white line are sensitive to both electronic and structural changes. In particular, the white line area is correlated with the density of unoccupied 5d states.[78,79] The adsorption of hydrogen causes partial filling of the Pt 5d states. Therefore, for Pt/SiO$_2$ in the hydrogen-rich atmospheres the white line intensities are smaller than for oxidized Pt particles of the same size, and even the bulk metal.[70] Upon transition to the ethylene-rich atmospheres, hydrogen is replaced by ethylene-derived carbonaceous species (by inference from the literature, mainly ethylidyne). Because these adsorbates are sterically more demanding (i.e., exhibit lower coverages) and the bonds are less polarized, the Pt 5d states are partially emptied, and thus, for Pt/SiO$_2$ in the ethylene-rich atmospheres the white line intensities are larger.

A theoretical study, based on a full multiple-scattering, self-consistent field, real-space Green's function approach,[80] showed for ultrasmall Pt particles pronounced effects of the particle morphology on the white line. For example, a distinctively less-intense white line was found for three-dimensional than for two-dimensional Pt$_7$ particles. The changes in the XAS spectra thus also may be partially due to particle reshaping, as might occur during the measurement sequence.

The peak at 9 eV above the absorption edge also has been observed in previous studies of bare and hydrogen-covered Pt particles on different supports[70,81,82] and attributed to transitions from the 2p$_{3/2}$ states to H 1s–Pt 5d antibonding states[70,81] or continuum resonances.[82] Also the peak at ≈32 eV is affected by the adsorption of hydrogen. The peak at 19 eV could be due to the irreversible adsorption of a specific form of carbonaceous species that also elicits a significant modification of the Pt–Pt bonding. The results discussed below support this latter inference in a more quantitative form.

Atomic Structure of the Catalysts Measured in Operando. For both supported catalysts, good EXAFS fits were obtained for all experimental conditions using the fitting models described in the Experimental section. As examples, the fits in k- and r-space in pure hydrogen and ethylene atmospheres are shown in Figures 5 and 6. The main fitting results are summarized in Figure 7 and Table 1. All fits and fitting results are given in the Supporting Information (Figures S7–S16).

For the Pd/SiO$_2$ catalyst, the energy shift, constrained for the whole measurement sequence, is $\Delta E_0 = -1.19 \pm 0.06$ eV. The coordination number in the forward sequence in the hydrogen-rich atmospheres is constant within the error bars, $n = 7.09 \pm 0.42$, decreases slightly at the transition, and increases gradually in the ethylene-rich atmospheres to a limiting value of 7.92 ± 0.44. In the backward sequence, very small changes in the coordination number are observed, with the exception of the transition, at which it increases to 8.64 ± 0.43. The Pd–Pd bond distance r in the forward sequence in the hydrogen-rich atmospheres is clearly larger than that of the bulk metal and decreases
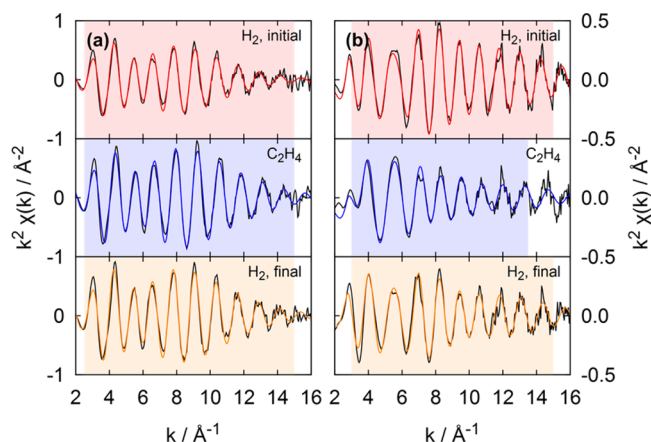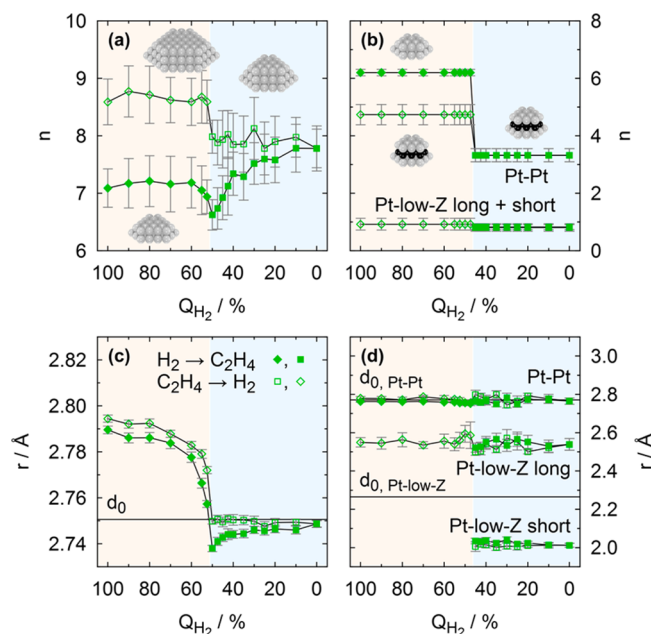
Figure 5. (a) k^2-weighted EXAFS oscillations $\chi(k)$ and best-fit results for Pd/SiO$_2$ in pure H$_2$ and C$_2$H$_4$, respectively. (b) Analog spectra for Pt/SiO$_2$. The highlighted areas show the fitting ranges.
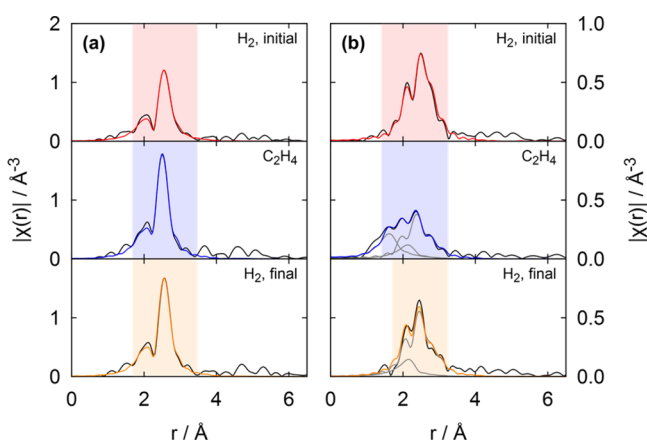
Figure 6. (a) Fourier-transform magnitudes $|\chi(r)|$ of the k^2-weighted EXAFS oscillations $\chi(k)$ and best-fit results for Pd/SiO$_2$ in pure H$_2$ and C$_2$H$_4$, respectively. (b) Analog spectra for Pt/SiO$_2$ showing the different contributions (Pt–Pt and Pt-low-Z long- and short-bond scattering paths, respectively). The highlighted areas show the fitting ranges.

Figure 7. Best-fit results of (a,b) the coordination numbers n and (c,d) the interatomic distances r for (a,c) Pd/SiO$_2$ (Pd−Pd scattering path) and (b,d) Pt/SiO$_2$ (Pt−Pt and Pt-low-Z long- and short-bond scattering paths, respectively) in different mixed atmospheres of H$_2$ and C$_2$H$_4$. Filled symbols indicate the forward sequence from pure H$_2$ to C$_2$H$_4$, and open symbols depict the backward sequence from C$_2$H$_4$ to H$_2$; diamonds are H$_2$-rich gas mixtures, and squares are C$_2$H$_4$-rich gas mixtures. Note that for Pt/SiO$_2$ the coordination numbers of both Pt-low-Z contributions are very similar and the Pt-low-Z long-bond contribution is only present in the C$_2$H$_4$-rich atmospheres.

gradually with the changing gas composition until a major bond length contraction (denoting the transition) occurs, and lastly, it increases again minimally in the ethylene-rich atmospheres to a limiting value of approximately that of the bulk metal. In the backward sequence, the Pd−Pd bond distances change very little in the ethylene-rich atmospheres, and only on reaching the hydrogen-rich atmospheres is a major bond lengthening evidenced. The general trends are thus reversible, albeit with some small hysteresis. The bond distances in the pure hydrogen atmospheres at the beginning and end of the measurement sequence are 2.790 ± 0.002 and 2.794 ± 0.002 Å (longer by 0.9 and 1.3%, respectively, as compared to the value of the bulk metal, 2.751 Å). The Debye−Waller factor σ^2 ranges between 0.008 and 0.010 Å^2, being larger in the hydrogen-rich and smaller in the ethylene-rich atmospheres. The r-factors are typically smaller than 0.01, indicative of the overall good fitting quality. The structural parameters obtained for the initial hydrogen-rich atmospheres are in good agreement with the results of an earlier EXAFS study (at the L$_3$-edge) of Pd/SiO$_2$ particles under similar conditions.[83]

The increased bond distances found in the hydrogen-rich atmospheres as compared to bulk palladium, the constant coordination numbers, and the increased Debye−Waller factors

as compared to the ethylene-rich atmospheres are indicative of the formation of a palladium hydride phase. Palladium incorporates hydrogen at random interstitial sites, causing lattice expansion and smaller distortions, but no transitions in the crystalline structure.[58] This has been confirmed in several EXAFS studies of supported Pd particles.[63,64,69,83]

The deintercalation and intercalation of hydrogen in the hydrogen-rich atmospheres during the forward and backward sequence, respectively, can be directly followed by the changes occurring in the bond distance. With the lattice expansion Δa and the bulk metal lattice constant a_0 the hydrogen content n of the palladium hydride phase PdH$_n$ can be determined via the subsequent equation, which has been shown to be valid over large pressure and temperature ranges:[84,85]

$$\Delta a \cdot a_0^{-1} = 0.0666n - 0.0164n^2 \tag{1}$$

The stoichiometries of the palladium hydride phases calculated using this equation do not directly correspond to the hydrogen content of the atmospheres in which the catalysts were present, indicating that they are strongly affected by the competitive adsorption of hydrogen and ethylene and the reactions that consume (or otherwise transform) them. For the pure hydrogen atmospheres at the beginning and end of the measurement sequence, hydrogen contents of $n = 0.156 \pm 0.027$ and 0.177 ± 0.025, respectively, are found, indicative of a mixed α- and β-palladium hydride phase.[58]

The magnitude of the lattice expansions in pure hydrogen atmospheres are in good agreement with previous results, considering the small particle sizes examined and low hydrogen pressure and temperature employed. For example, for Pd

Table 1. Best-Fit Parameters Obtained in the EXAFS Fitting for Pd/SiO$_2$ and Pt/SiO$_2$

Pd/SiO$_2$			
Pd-Pd path			
	H$_2$-rich, forward	C$_2$H$_4$-rich, forward	C$_2$H$_4$-rich, backward	H$_2$-rich, backward
ΔE_0 / eV	-1.191 ± 0.063			
n	7.09 ± 0.41	7.24 ± 0.38	7.92 ± 0.44	8.64 ± 0.43
r / Å	2.776 ± 0.002	2.744 ± 0.002	2.750 ± 0.002	2.786 ± 0.002
σ^2 / Å^2	$(98.0\pm4.3)\cdot10^{-4}$	$(82.9\pm3.5)\cdot10^{-4}$	$(84.5\pm3.7)\cdot10^{-4}$	$(91.9\pm3.5)\cdot10^{-4}$
r-factor	$(9.6\pm2.4)\cdot10^{-3}$	$(7.6\pm1.2)\cdot10^{-3}$	$(8.0\pm0.8)\cdot10^{-3}$	$(7.2\pm0.5)\cdot10^{-3}$

Pt/SiO$_2$			
Pt-Pt path			
	H$_2$-rich, forward	C$_2$H$_4$-rich, forward	C$_2$H$_4$-rich, backward	H$_2$-rich, backward
ΔE_0 / eV	8.192 ± 0.230			
n	6.20 ± 0.11	3.32 ± 0.23		4.74 ± 0.35
r / Å	2.760 ± 0.004	2.762 ± 0.018	2.777 ± 0.020	2.776 ± 0.012
σ^2 / Å^2	$(74.8\pm1.8)\cdot10^{-4}$	$(77.6\pm5.1)\cdot10^{-4}$	$(77.0\pm6.0)\cdot10^{-4}$	$(81.5\pm5.0)\cdot10^{-4}$
$\sigma^{(3)}$ / Å^3	$(224.3\pm48.6)\cdot10^{-6}$	$(759.8\pm252.0)\cdot10^{-6}$	$(902.5\pm301.7)\cdot10^{-6}$	$(550.2\pm158.1)\cdot10^{-6}$
Pt-low-Z long-bond path			
	H$_2$-rich, forward	C$_2$H$_4$-rich, forward	C$_2$H$_4$-rich, backward	H$_2$-rich, backward
ΔE_0 / eV	8.192 ± 0.230			
n		0.81 ± 0.13		0.92 ± 0.20
r / Å		2.539 ± 0.031	2.510 ± 0.026	2.549 ± 0.037
σ^2 / Å^2		$(22.0\pm33.0)\cdot10^{-4}$	$(26.1\pm34.9)\cdot10^{-4}$	$(67.1\pm55.5)\cdot10^{-4}$
Pt-low-Z short-bond path			
	H$_2$-rich, forward	C$_2$H$_4$-rich, forward	C$_2$H$_4$-rich, backward	H$_2$-rich, backward
ΔE_0 / eV	8.192 ± 0.230			
n		0.83 ± 0.09		
r / Å		2.023 ± 0.013	2.011 ± 0.016	
σ^2 / Å^2		$(86.5\pm21.1)\cdot10^{-4}$	$(96.5\pm27.0)\cdot10^{-4}$	
r-factor	$(8.4\pm2.7)\cdot10^{-3}$	$(8.8\pm3.5)\cdot10^{-3}$	$(11.8\pm6.5)\cdot10^{-3}$	$(15.2\pm3.1)\cdot10^{-3}$

particles with sizes of 1−2 nm on multiple supports at atmospheric pressure and room temperature, lattice expansions of ≤ 1.8% have been reported.[69] For 5 wt % Pd/Al$_2$O$_3$ with sizes of ≈5 nm, an expansion of 3.7% was found,[63] and for Pd/SiO$_2$ with sizes of 1.9−10.8 nm at 250 °C, relatively larger expansions of 5−7% have been identified.[66]

The pronounced and abrupt structural transition between the hydrogen- and ethylene-rich atmospheres can be explained by changes occurring in the bonding states of reactant-derived species to the palladium particles. In the hydrogen-rich atmospheres, the ethylene is consumed in the hydrogenation reaction and atomic hydrogen is the dominant species on (and within) the Pd particles, whereas in the ethylene-rich atmospheres, both surface- and bulk-absorbed hydrogen are depleted, and an ethylidyne layer forms as a result. This causes an increase in the structural order of the palladium particles due to the loss of the distribution of bond strains that results from the deintercalation of the H bound in the form of a metal hydride.[86] As noted above, and contrary to the expectation that an ethylidyne layer would lead to Pd-low-Z contributions, it is not possible to establish with statistical significance the nature of any form of Pd−C bonding that may be present. Such interactions (e.g., from ethylidyne) must exist, but likely, embed levels of disorder that make them hard to fit. In an earlier study of 3.5 nm Pd/C particles, heating in ethylene at 150 °C for 20 min resulted in the formation of a palladium carbide phase (PdC$_n$) with a Pd−Pd bond distance expanded by 1.2% as compared to the bulk metal, indicative of a carbon content of $n = 0.06$.[64] In contrast, for analogous Pd/Al$_2$O$_3$ particles, the formation of a palladium carbide phase was not observed. Instead, a similar behavior was identified as is found here.[64]

When taken together, the results (i.e., the increasing coordination numbers and bond distances) conclusively show that the particles grow considerably and their structure changes

within the ethylene-rich atmospheres. This process could be mediated by highly mobile molecular ethylidyne-palladium complexes. The high mobility of ethylidyne on Pt(111) surfaces at room temperature has been confirmed in STM studies,[47,48,87] but such dynamics have not been correlated with mechanisms of particle coarsening to this point, a subject that might be addressed in future research.

The mechanism underlying the increase in coordination number at the transition between the ethylene- to the hydrogen-rich atmospheres remains poorly understood. The STEM data unambiguously establish that the effects are directly correlated with significant coarsening of the supported Pd clusters. The mobility of the Pd atoms involved, whatever the nature of the mechanism that sustains it, must be substantial.

For the Pt/SiO$_2$ catalyst, very different qualitative and quantitative behavior is found. The energy shift, constrained for the scattering paths in all spectra, is $\Delta E_0 = 8.19 \pm 0.23$ eV. The Pt−Pt coordination number found in the initial hydrogen-rich atmospheres is $n = 6.20 \pm 0.11$, in the ethylene-rich atmospheres 3.32 ± 0.23, and in the final hydrogen-rich atmospheres 4.74 ± 0.35. These are substantial changes in the bonding habits of the nanoscale Pt clusters. Unlike the Pd clusters, substantial contributions from Pt-low-Z bonding are evidenced, a form of bonding that becomes pronounced only after the sample is immersed in ethylene-rich atmospheres. Two distinct forms of Pt-low-Z bonding (a long and short bond, respectively) are evidenced. Only one of these (the long bond) is retained when the sample is returned to a hydrogen-rich ambient. The Pt-low-Z long-bond coordination number is in the ethylene-rich atmospheres 0.81 ± 0.13 and in the final hydrogen-rich atmospheres 0.92 ± 0.20, the Pt-low-Z short-bond coordination number in the ethylene-rich atmospheres is 0.83 ± 0.09. The bond distances of the Pt−Pt and the two Pt-low-Z contributions seem to be essentially constant during the whole measurement

sequence. The Pt−Pt bond distance in the initial hydrogen-rich atmospheres is $r = 2.760 \pm 0.004$ Å (i.e., slightly smaller than that of the bulk metal of 2.772 Å) and then seems to increase only minimally thereafter. The bond distances of the Pt-low-Z contributions are 2.52 and 2.02 Å, respectively. The Debye−Waller factors, σ^2, are similar for all three contributions, typically slightly smaller than 0.01 Å^2, and smallest in the initial hydrogen-rich, largest in the ethylene-rich, and intermediate in the final hydrogen-rich atmospheres. The third cumulant $\sigma^{(3)}$ of the Pt−Pt contribution, ranging between 220 and 760×10^{-6} Å, shows a similar dependence. These data reveal, again, a striking structural complexity within the bonding dynamics of the supported metal clusters—dynamics with marked "in operando" sensitivities. Their nature is discussed in detail in the section that follows.

It is interesting to note that, in the initial hydrogen-rich atmospheres, significant metal−support interactions are not evidenced, as can be inferred from the absence of Pt-low-Z bonding contributions. This is in contrast to the results of several previous EXAFS studies of Pt/SiO$_2$ particles in hydrogen atmospheres, in which Pt-low-Z contributions at 1.9−2.2 Å (i.e., short-bond contributions) were identified and attributed to Pt-support-O bonds.[70,72,88] The discrepancy may be attributed to the different particle structures and experimental conditions (typically, larger particles, reduced at higher temperatures, have been used in the earlier work). In another study, for Pt/SiO$_2$ particles with comparable structures under similar experimental conditions as are examined here, no discernible contributions from metal−support interactions were found.[71] Moreover, the Pd/SiO$_2$ catalysts described above were treated in the same manner and also showed no significant contributions due to metal−support interactions in the EXAFS data. The Pt−Pt coordination number, a parameter indicative of the average particle structure, is very similar in the initial hydrogen-rich atmospheres to those identified in EXAFS studies for supported Pt particles with similar TEM sizes.[70,71] The slight bond compression as compared to the bulk metal is a finite-size effect well-known for Pt particles smaller than ≈2 nm.[89]

The Pt-low-Z contributions, which form upon transition to the ethylene-rich atmospheres, can in principle be due to metal−support or metal−adsorbate interactions. The short-bond contribution is most probably due to Pt−C bonding of ethylene-derived species (i.e., mainly ethylidyne) adsorbed on the Pt particles, because it is reversibly formed and only prevalent within the ethylene-rich atmospheres. In addition, DFT calculations of ethylidyne adsorbed on (111) surfaces of different Pt clusters yield very similar Pt−C bond distances, with values ranging between 1.96−2.02 Å.[90−92] The long-bond contribution has two possible origins; either it is due to intraparticle Pt−C bonding or Pt−O bonding to the support. It is not possible to distinguish between Pt−C and Pt−O bonding with EXAFS. Given that this species only forms upon exposure to ethylene-rich atmospheres, the assignment to a Pt−C-based bonding motif seems most likely, a point that is discussed in terms of a structural model in the section below. To our knowledge, Pt-low-Z long-bond contributions of this type have not been identified in previous studies for SiO$_2$ supports. The only similar findings were for Al$_2$O$_3$ supported clusters; their physical origin was not fully explained.[72,93] In contrast, Pt-low-Z short-bond contributions have been observed frequently for SiO$_2$ supports and typically attributed to Pt−O bonding to the support (see above).[70,72,88,93] The results presented here suggest that the nature of this bonding may require a careful individual assessment.

Despite the fact that a number of prior studies have used EXAFS to investigate the structures adopted by supported Pt clusters in an ethylene atmosphere,[71,72] the correlation that might exist between their reactivity and structural properties remain incompletely understood. For Pt/Al$_2$O$_3$ particles with similar sizes,[71,72] analogous results were obtained as are reported here—pronounced differences between the spectra in hydrogen and ethylene atmospheres, in agreement with a decrease of the Pt−Pt and an increase of the Pt-low-Z bonding contributions. In contrast, for larger Pt/SiO$_2$ particles,[72] only minor differences between hydrogen and ethylene atmospheres were identified. This might be expected due to their more bulk-like bonding habits. As cluster size strongly weights the contribution of surface atoms in XAS, such differences may underlay much of the variability evidenced in the current literature. The nature of the surface and interior cluster bonding habits is an attribute that critically distinguishes the quantitative structural model described above. What is crucial to note here is that the nature of the processes that impact the Pt−Pt bonding, engendering a pronounced and only partially reversible decrease in coordination number due to the exposure to an ethylene-rich ambient, is constrained by the STEM data. As noted above, only small (if any) changes in the Pt cluster-size distribution occur over the course of the in operando experiment. For this reason, it seems necessary to reason that the changes in bonding (e.g., in coordination numbers and Debye−Waller factors) seen in the structural transitions occurring between the hydrogen- and ethylene-rich atmospheres and vice versa are not due to redispersion of the particles, but rather, they may in fact result from changes in their chemical composition, a point explored in more detail below.

In summary, for Pt/SiO$_2$ qualitatively similar changes occur during the experiment as for Pd/SiO$_2$, with exception of the hydrogen (de)intercalation and the significant apparent decrease in particle size upon the transition from hydrogen- to ethylene-rich atmospheres in the forward sequence. In the following section, models that quantitatively account for these features will be discussed.

Comparison Between the Mechanisms of Structural Transformation of the Two Catalysts. The results of the EXAFS fitting (in particular, the average M−M coordination numbers) and the STEM analysis (the particle sizes) can be interpreted self-consistently in terms of the structural models given in Figure 7 and the Supporting Information (Table S1).

The changes in the Pd/SiO$_2$ catalyst in the different mixed hydrogen and ethylene atmospheres during the measurement sequence can be attributed to modifications made in the morphology of the particles rather than their chemical composition. Because a mechanism involving hydrogen (de)intercalation mainly affects the crystalline structure (i.e., bond distances, order), but not the overall morphology (i.e., metal atom number and coordination), and given that no contributions from other species are evidenced, particle growth must occur in this instance. The average particle morphology is, considering both the results of the EXAFS fitting and the STEM analysis and under the assumption that the particles exhibit ideal truncated-cuboctahedral shapes, in the initial hydrogen-rich atmospheres in best agreement with a bilayer consisting of 45 atoms, in the ethylene-rich atmospheres under equilibrium conditions with a trilayer of 82 atoms, and in the final hydrogen-rich atmospheres with a trilayer of 145 atoms (Figure 7a). During the measurement sequence, the particles grow, based on the number of atoms present in the model particles, by a factor of ≈3.2. This corresponds to a

decrease in total surface area by a factor of ≈2.3. These models are clearly gross simplifications, neglecting important features (e.g., small particles often exhibit perturbed, nonideal structures, and the coordination numbers and particle sizes agree with multiple model structures). Still, when taken together, the data clearly evidence the important mechanistic role of particle coarsening that is gas composition-sensitive for the Pd/SiO$_2$ catalysts, a substantial (and irreversible) growth of the catalyst clusters during ethylene hydrogenation that becomes most pronounced in ethylene-rich regimes. Small particles appear to be especially susceptible to this form of restructuring. How effects such as bond strains and adsorbate-induced bonding influence this coarsening will need to be addressed in future studies.

For the Pt/SiO$_2$ catalyst, a very different behavior is identified. Initially in the hydrogen-rich atmospheres, the particles are purely metallic and thus, under the assumptions stated above, in best agreement with a bilayer comprised of ~31 atoms (Figure 7b). The exposure to an ethylene-rich atmosphere leads to pronounced changes in the chemical composition of the Pt clusters, an impact most strongly evidenced by the appearance of significant contributions from two distinct forms of Pt-low-Z bonding. Specifically, these two additional bonding contributions can be attributed to ethylidyne adsorbed on the particles and a Pt–C species on (but more likely, within) the particles, respectively. Upon returning to hydrogen-rich atmospheres, only the contribution due to the Pt–C species persists. How the adoption of a specific form of Pt–C bonding can rationalize, at least in good qualitative terms, all the features observed experimentally is illustrated in schematic form in Figure 7. Several aspects of the experimental results inform the model presented there. In considering only the changes in the Pt–Pt bonding upon altering the gas from hydrogen- to ethylene-rich compositions (the dramatic decrease in Pt–Pt coordination numbers), a simple model might invoke processes that degrade the initial three-dimensional morphologies of the metal clusters in ways that lead to the formation of smaller, essentially two-dimensional rafts (from a truncated-cuboctahedral 31-atom cluster to a 7-atom raft-like cluster). This transition in the cluster motif would have to be partially reversible in that the return from an ethylene- to hydrogen-rich gas composition is associated with a pronounced increase in the M–M coordination numbers, which quantitatively suggests within this model some degree of coarsening (e.g., from a 7- to a 19-atom raft). Substantive arguments weigh against this model, however. First, it is hard to rationalize M–M bonding dynamics that would first decompose a nanoscale cluster and then partially revert solely on the basis of a change in gas phase. Second, and most significantly, no Z-contrast differences are evidenced in the STEM images of the pristine catalyst particles and those recovered after the XAS experiment. Two-dimensional rafts, even if having similar lateral sizes, would have a much lower Z-contrast than three-dimensional particles given their lower Pt-atom content. Another possibility to explain the results is to assume that the particle size distribution changed during the reaction. Without an in operando STEM experiment that would provide statistical information about the particle size distributions present before, during, and after the reaction sequence, all that can be definitively concluded is that the sample motifs and size distributions are indistinguishable when quantitatively evaluated by STEM before and after the XAS measurements. This argues strongly against any model that involves a massive dismemberment of the M–M bonding and redistribution of the mass present in the metal clusters. When considering mechanisms that might elicit changes in the chemical composition of

the Pt clusters, a more sophisticated model of the catalysts structural evolution during the measurement sequence emerges. This model (as depicted in Figure 7b) is based on competitive partitioning of ethylene in the olefin-rich atmospheres along pathways forming ethylidyne and a carbide-like phase, each moiety contributing a distinct form of Pt-low-Z bonding. The model structure adopted to facilitate this consideration, a Pt$_{31}$C$_{12}$ cluster (Figure 7b), is derived from the original, truncated-cuboctahedral Pt$_{31}$ cluster by intercalation of a C atom layer between the two Pt atom layers and describes the state of the catalyst in the final hydrogen-rich atmospheres. This structure is based on a modified zinc blende structure, which is predicted in theoretical calculations to be the stable platinum carbide phase under ambient conditions.[94,95] The cluster exhibits the highest possible symmetry based on this structural motif.

This model, while providing a good qualitative description of the trends seen in the XAS data, does not fully reproduce it quantitatively. For example, the first-shell M–M coordination number (4.26) is smaller and the Pt–C bonding contribution (1.55) larger than that observed experimentally. In particular, the coordination number of the Pt–C long-bond would correspond to only 6–9 C atoms, rather than a full layer, being present within the cluster. These quantitative discrepancies notwithstanding, the proposed model structure should be considered as representing only an upper limit of C content of a platinum carbide phase and illustrative of a chemically plausible mechanism through which the M–M coordination numbers of the supported Pt clusters can be decreased markedly without requiring their effective dissociation. It should also be noted that the coordination number of the Pt-low-Z short-bond contribution is in reasonable agreement with the expectations for an ideal full-coverage ethylidyne adlayer (i.e., 1/4 ML[47,48,87]), as forms on a single-crystalline Pt(111) surface. Considering the high fraction of Pt surface atoms (24/31 = 0.774), which, within the model, does not change significantly during the measurement sequence, the ideal ethylidyne coverage is 24/31 × 3/4 = 0.58. It is likely, however, that the actual ethylidyne coverage for these nanoparticles could be higher than for single crystal surfaces, because they exhibit a three-dimensional surface structure exposing a broader diversity of active bonding sites. The increase in the M–M coordination number that occurs on cycling from the ethylene- to the hydrogen-rich atmospheres is most likely due to a structural relaxation mediated by the removal of the bound ethylidyne groups via an H-addition-mediated desorption pathway. A partial decomposition of the platinum carbide phase can be excluded with certainty, because the coordination number of the Pt-low-Z long-bond contribution is unaffected.

Additional support for the carbide-phase model presented in Figure 7b comes from the attributes of electronic structure revealed in the XANES data. During the measurement sequence, the exposure to mixed hydrogen and ethylene atmospheres leads to an intriguing evolution of the white line intensities for the Pt/SiO$_2$ catalysts, a pronounced increase occurring in the olefin-rich gas composition that is retained when the sample is returned to a hydrogen-rich ambient. This effect is further correlated with the presence/retention of the long Pt–C bonding contribution. Most significantly, the formation of the new phase, embedding carbide-like Pt–C bonds, fully rationalizes this feature and the retention of the significant white line intensity upon returning from ethylene- to hydrogen-rich atmospheres. It is thus the platinum carbide speciation (and most likely not ethylidyne, which is removed by exposure to hydrogen) which provides the modifications in the electronic structure underlying this effect.

It seems particularly important that future work should more fully explore how carbon is incorporated into these supported metal catalysts and whether the very small particle sizes facilitate this in some way. We believe that studies to this end will likely require both new analytical and theoretical capabilities providing information about the development of the atomic and electronic structure of single particles during catalytic reaction.

CONCLUSIONS

We describe in this perspective the properties exhibited by two exemplary catalysts, Pd/SiO_2 and Pt/SiO_2, as evidenced during ethylene hydrogenation in various mixed atmospheres of hydrogen and ethylene using in operando X-ray absorption spectroscopy (XAS). Both catalysts were found to undergo major, atomic-scale, structural transformations and pronounced changes in electronic properties. Specifically, a defined transition between hydrogen- and hydrocarbon-covered surfaces was identified and varying composition-dependent transformations of the metal structures. For Pd/SiO_2, gradual, gas-phase composition-dependent hydrogen (de)intercalation was observed, an aspect of the dynamics that is strongly affected by the competitive adsorption of hydrogen and ethylene and their surface reactions. More crucially, though, the Pd clusters of this catalyst showed a pronounced tendency to coarsen during hydrogenation, an attribute that also shows pronounced sensitivity to the gas-composition-mediated phase transformations seen in this system. This seems to be a feature that theoretical models of the nanoscale mechanics might be developed to address.

The chemistry of the Pt-based catalysts displays a central role of the composition-driven structural transformations. Here no significant coarsening is observed, but rather, a change in the structural features of the metal phase is mediated by the formation of essentially carbide-like materials. This unexpected dynamical form of structural complexity, however, has no consequential effect on the overall reactivity—the ethylene hydrogenation proceeds completely, regardless of the metal cluster catalyst's structure, composition, and size. This evidence is an intriguing addition that might be made to the classical metric used to define the structural sensitivity of a heterogeneous catalytic process. In this case, olefin hydrogenation provides a remarkable example of how significant forms of complexity in atomic and electronic structural dynamics can be embedded within otherwise apparently simple structure−property correlations in catalysis.

In this perspective, we have highlighted the use of an essential tool of in operando characterization in a study of an exemplary, and arguably exceptionally well-investigated, catalytic reaction. These data illustrate how, even in a system such as this, there remain challenging and as yet poorly understood features of atomic and electronic structure, as well as the dynamics that shape them, which future work must come to address to allow progress to be made against grand challenges, most notably to use established principles of materials structure and dynamics to guide the synthesis of new catalysts. An opportunity exists to make progress in research in ways that will make it possible to develop such principles and with a depth of understanding that has not been possible in the past. Our work has emphasized the role of X-ray spectroscopy (XANES and EXAFS) as an essential experimental tool for use in developing fundamental understanding of structure and dynamics in heterogeneous catalysis, in particular as a means for building via in operando investigations the science needed to address attributes of nanoscale structure as

they exist and are transformed in real-process conditions. It is becoming increasingly evident that the sophistication/complexity of the questions being addressed in research challenge the capabilities of even state-of-the-art experimental and theoretical methods. Considering the presented data as an explicit example, the depth of detail that can be extracted from analyses of that data very much follows directly from the quantitative attributes of the XANES and EXAFS measurements. To better understand the reaction dynamics, as well as the mechanisms of metal-cluster coarsening and fragmentation evidenced there, enhancements of spatiotemporal and energy resolutions are highly desirable.[96−99] The enhancement of spatial resolution would also stand as an advancement of capability of the most urgent importance as it is in principle the only means that will allow a circumvention of the limitation of XAS as an ensemble-averaging spectroscopic method—which for measurements made neglecting of the details of cluster disorder, as well as distributions of size, composition, and shape, could lead to spurious analytical assessments.[86,100−103] The improvement of energy resolution has recently become possible with the utilization of High Energy Resolution Fluorescence Detection (HERFD) methods,[104−109] in which only selected emission lines are detected, resulting in more sharp and intense XANES features compatible with rigorous treatments by theory, as well as an enhanced sensitivity in the EXAFS range,[110] which, most importantly, can be used to develop new understandings of in operando materials dynamics in catalysis.[105,108,111] These methods are becoming progressively more attractive to the catalysis community, and their use will, in turn, continue to stimulate the development of both new and more powerful synchrotron sources, as well as new types of synchrotron-based techniques for use in operando catalysis research.

ASSOCIATED CONTENT

ⓢ Supporting Information

The following file is available free of charge on the ACS Publications website at DOI: 10.1021/cs501846g.

> Additional facts related to ethylene and hydrogen adsorption, ethylene hydrogenation, and palladium hydrides, as well as information about the experimental methods and results of the STEM and XAFS experiments are included (PDF)

AUTHOR INFORMATION

Corresponding Authors
*E-mail: anatoly.frenkel@yu.edu.
*E-mail: r-nuzzo@illinois.edu.
Notes
The authors declare no competing financial interest.

ACKNOWLEDGMENTS

REFERENCES

(1) Ertl, G.; Knözinger, H.; Weitkamp, J. *Handbook of Heterogeneous Catalysis*; Wiley-VCH GmbH & Co. KGaA: Weinheim, 1997; pp 1277−1285.

(2) Corain, B.; Schmid, G.; Toshima, N. *Metal Nanoclusters in Catalysis and Materials Science: The Issue of Size Control*; Elsevier B.V.: Amsterdam, 2007; pp 3−20.

(3) Chorkendorff, I.; Niemantsverdriet, J. W. *Concepts of Modern Catalysis and Kinetics*; John Wiley & Sons, Inc.: New York, 2003; pp 1−21.

(4) Rioux, R. M. *Model Systems in Catalysis*; Springer: Berlin, 2010; pp 253−367.

(5) Stoltze, P.; Nørskov, J. K. *Phys. Rev. Lett.* **1985**, *55*, 2502−2505.

(6) Schloegl, R.; Schoonmaker, R. C.; Muhler, M.; Ertl, G. *Catal. Lett.* **1988**, *1*, 237−241.

(7) Imbihl, R.; Behm, R. J.; Schlögl, R. *Phys. Chem. Chem. Phys.* **2007**, *9*, 3459−3459.

(8) Sabatier, P. *La Catalyse en chimie organique*; C. Beranger: Paris, 1913; pp 105−113.

(9) Wijngaarden, R. J.; Kronberg, A.; Westerterp, K. R. *Industrial Catalysis: Optimizing Catalysts and Processes*; John Wiley & Sons, Inc.: New York, 2007; pp 1−8.

(10) Hagen, J. *Industrial Catalysis*. John Wiley & Sons, Inc.: New York, 2005; pp 59−82.

(11) Bond, G. C. *Metal-Catalysed Reactions of Hydrocarbons*; Springer: Berlin, 2005; pp 395−435.

(12) Bond, G. C.; Phillipson, J. J.; Wells, P. B.; Winterbottom, J. M. *Trans. Faraday Soc.* **1964**, *60*, 1847−1864.

(13) Salmeron, M.; Somorjai, G. A. *J. Phys. Chem.* **1982**, *86*, 341−350.

(14) Lee, I.; Zaera, F. *J. Catal.* **2010**, *269*, 359−366.

(15) Bos, A. N. R.; Botsma, E. S.; Foeth, F.; Sleyster, H. W. J.; Westerterp, K. R. *Chem. Eng. Process.* **1993**, *32*, 53−63.

(16) Bos, A. N. R.; Westerterp, K. R. *Chem. Eng. Process.* **1993**, *32*, 1−7.

(17) Borodziński, A.; Cybulski, A. *Appl. Catal., A* **2000**, *198*, 51−66.

(18) Morales, R.; Zaera, F. *J. Phys. Chem. B* **2006**, *110*, 9650−9659.

(19) Morales, R.; Zaera, F. *J. Phys. Chem. C* **2007**, *111*, 18367−18375.

(20) National Standard Reference Data Series (NSRDS)Horiuti, J.; Miyahara, K. *Hydrogenation of Ethylene on Metallic Catalysts*. NSRDS-NBS 13, 1968; pp 1−62.

(21) Zaera, F.; Somorjai, G. A. *J. Am. Chem. Soc.* **1984**, *106*, 2288−2293.

(22) Zaera, F.; Somorjai, G. A. *J. Phys. Chem.* **1985**, *89*, 3211−3216.

(23) De la Cruz, C.; Sheppard, N. *J. Mol. Struct.* **1991**, *247*, 25−30.

(24) Beebe, T. P.; Yates, J. T. *J. Phys. Chem.* **1987**, *91*, 254−257.

(25) Beebe, T. P., Jr; Albert, M. R.; Yates, J. T., Jr *J. Catal.* **1985**, *96*, 1−11.

(26) Beebe, T. P.; Yates, J. T. *J. Am. Chem. Soc.* **1986**, *108*, 663−671.

(27) Hill, J. M.; Shen, J.; Watwe, R. M.; Dumesic, J. A. *Langmuir* **2000**, *16*, 2213−2219.

(28) Binder, A.; Seipenbusch, M.; Muhler, M.; Kasper, G. *J. Catal.* **2009**, *268*, 150−155.

(29) Briggs, D.; Dewing, J.; Burden, A. G.; Moyes, R. B.; Wells, P. B. *J. Catal.* **1980**, *65*, 31−35.

(30) Soma, Y. *J. Catal.* **1982**, *75*, 267−274.

(31) Mohsin, S. B.; Trenary, M.; Robota, H. J. *J. Phys. Chem.* **1988**, *92*, 5229−5233.

(32) Mohsin, S. B.; Trenary, M.; Robota, H. J. *Chem. Phys. Lett.* **1989**, *154*, 511−515.

(33) Wasylenko, W.; Frei, H. *J. Phys. Chem. B* **2005**, *109*, 16873−16878.

(34) Sinfelt, J. H. *J. Phys. Chem.* **1964**, *68*, 856−860.

(35) Dorling, T. A.; Eastlake, M. J.; Moss, R. L. *J. Catal.* **1969**, *14*, 23−33.

(36) Briggs, D.; Dewing, J. *J. Catal.* **1973**, *28*, 338−339.

(37) Schlatter, J. C.; Boudart, M. *J. Catal.* **1972**, *24*, 482−492.

(38) Cortright, R. D.; Goddard, S. A.; Rekoske, J. E.; Dumesic, J. A. *J. Catal.* **1991**, *127*, 342−353.

(39) De La Cruz, C.; Sheppard, N. *Phys. Chem. Chem. Phys.* **1999**, *1*, 329−332.

(40) Shen, J.; Hill, J. M.; Watwe, R. M.; Spiewak, B. E.; Dumesic, J. A. *J. Phys. Chem. B* **1999**, *103*, 3923−3934.

(41) Cremer, P. S.; Somorjai, G. A. *J. Chem. Soc., Faraday Trans.* **1995**, *91*, 3671−3677.

(42) Öfner, H.; Zaera, F. *J. Phys. Chem. B* **1997**, *101*, 396−408.

(43) Rekoske, J. E.; Cortright, R. D.; Goddard, S. A.; Sharma, S. B.; Dumesic, J. A. *J. Phys. Chem.* **1992**, *96*, 1880−1888.

(44) Zaera, F. *Phys. Chem. Chem. Phys.* **2013**, *15*, 11988−12003.

(45) Tilekaratne, A.; Simonovis, J. P.; López Fagúndez, M. F.; Ebrahimi, M.; Zaera, F. *ACS Catal.* **2012**, *2*, 2259−2268.

(46) Okada, T.; Kim, Y.; Sainoo, Y.; Komeda, T.; Trenary, M.; Kawai, M. *J. Phys. Chem. Lett.* **2011**, *2*, 2263−2266.

(47) Land, T. A.; Michely, T.; Behm, R. J.; Hemminger, J. C.; Comsa, G. *Appl. Phys. A: Mater. Sci. Process.* **1991**, *53*, 414−417.

(48) Land, T. A.; Michely, T.; Behm, R. J.; Hemminger, J. C.; Comsa, G. *J. Chem. Phys.* **1992**, *97*, 6774−6783.

(49) Cremer, P.; Stanners, C.; Niemantsverdriet, J. W.; Shen, Y. R.; Somorjai, G. *Surf. Sci.* **1995**, *328*, 111−118.

(50) Cremer, P. S.; Su, X.; Shen, Y. R.; Somorjai, G. A. *J. Am. Chem. Soc.* **1996**, *118*, 2942−2949.

(51) Cremer, P.; Su, X.; Shen, Y. R.; Somorjai, G. *Catal. Lett.* **1996**, *40*, 143−145.

(52) Horiuti, I.; Polanyi, M. *Trans. Faraday Soc.* **1934**, *30*, 1164−1172.

(53) Zaera, F. *J. Am. Chem. Soc.* **1989**, *111*, 8744−8745.

(54) Stacchiola, D.; Azad, S.; Burkholder, L.; Tysoe, W. T. *J. Phys. Chem. B* **2001**, *105*, 11233−11239.

(55) Laidler, K. J.; Wall, M. C.; Markham, M. C. *J. Chem. Phys.* **1953**, *21*, 949−950.

(56) Janssens, T. V. W.; Stone, D.; Hemminger, J. C.; Zaera, F. *J. Catal.* **1998**, *177*, 284−295.

(57) Davis, S. M.; Zaera, F.; Gordon, B. E.; Somorjai, G. A. *J. Catal.* **1985**, *92*, 240−246.

(58) Manchester, F. D.; San-Martin, A.; Pitre, J. M. *J. Phase Equilib.* **1994**, *15*, 62−83.

(59) Daley, S. P.; Utz, A. L.; Trautman, T. R.; Ceyer, S. T. *J. Am. Chem. Soc.* **1994**, *116*, 6001−6002.

(60) Als-Nielsen, J.; McMorrow, D. *Elements of Modern X-Ray Physics*; John Wiley & Sons, Ltd.: New York, 2001; pp 242−260.

(61) Bunker, G. *Introduction to XAFS - A Practical Guide to X-ray Absorption Fine Structure Spectroscopy*; Cambridge Unviersity Press: Cambridge, U.K., 2010, pp 8−33.

(62) Rodriguez, J. A.; Hanson, J. C.; Chupas, P. J. *In-situ Characterization of Heterogeneous Catalysts*; John Wiley & Sons, Inc.: New York,2013; pp 121−473.

(63) Davis, R. J.; Landry, S. M.; Horsley, J. A.; Boudart, M. *Phys. Rev. B* **1989**, *39*, 10580−10583.

(64) McCaulley, J. A. *J. Phys. Chem.* **1993**, *97*, 10372−10379.

(65) McCaulley, J. A. *Phys. Rev. B* **1993**, *47*, 4873−4879.

(66) Kochubey, D. I.; Feodorov, V. K.; Williams, C.; Nogin, Y. N.; Stenin, M. V.; Ryndin, Y. A.; Thomas, J. M.; Zamaraev, K. I. *Catal. Lett.* **1990**, *5*, 349−352.

(67) Kubota, T.; Kitajima, Y.; Asakura, K.; Iwasawa, Y. *Bull. Chem. Soc. Jpn.* **1999**, *72*, 673−681.

(68) Lin, C.-M.; Hung, T.-L.; Huang, Y.-H.; Wu, K.-T.; Tang, M.-T.; Lee, C.-H.; Chen, C. T.; Chen, Y. Y. *Phys. Rev. B* **2007**, *75* (125426), 1−6.

(69) Tew, M. W.; Miller, J. T.; Bokhoven, J. A. v. *J. Phys. Chem. C* **2009**, *113*, 15140−15147.

(70) Reifsnyder, S. N.; Otten, M. M.; Sayers, D. E.; Lamb, H. H. *J. Phys. Chem. B* **1997**, *101*, 4972−4977.

(71) Bus, E.; Ramaker, D. E.; Bokhoven, J. A. v. *J. Am. Chem. Soc.* **2007**, *129*, 8094−8102.

(72) Alexeev, O. S.; Li, F.; Amiridis, M. D.; Gates, B. C. *J. Phys. Chem. B* **2004**, *109*, 2338−2349.

(73) Clausen, B. S.; Steffensen, G.; Fabius, B.; Villadsen, J.; Feidenhans'l, R.; Topsøe, H. *J. Catal.* **1991**, *132*, 524−535.

(74) Newville, M. *J. Synchrotron Radiat.* **2001**, *8*, 322−324.

(75) Ravel, B.; Newville, M. *J. Synchrotron Radiat.* **2005**, *12*, 537−541.

(76) Brown, M.; Peierls, R. E.; Stern, E. A. *Phys. Rev. B* **1977**, *15*, 738−744.

(77) Mansour, A. N.; Cook, J. W.; Sayers, D. E. *J. Phys. Chem.* **1984**, *88*, 2330−2334.

(78) Lytle, F. W. *J. Catal.* **1976**, *43*, 376−379.

(79) Lytle, F. W.; Wei, P. S. P.; Greegor, R. B.; Via, G. H.; Sinfelt, J. H. *J. Chem. Phys.* **1979**, *70*, 4849−4855.

(80) Ankudinov, A. L.; Rehr, J. J.; Low, J. J.; Bare, S. R. *J. Chem. Phys.* **2002**, *116*, 1911−1919.

(81) Samant, M. G.; Boudart, M. *J. Phys. Chem.* **1991**, *95*, 4070−4074.

(82) Asakura, K.; Kubota, T.; Chun, W. J.; Iwasawa, Y.; Ohtani, K.; Fujikawa, T. *J. Synchrotron Radiat.* **1999**, *6*, 439−441.

(83) Tew, M. W.; Miller, J. T.; Bokhoven, J. A. v. *J. Phys.: Conf. Ser.* **2009**, *190* (012172), 1−5.

(84) Feenstra, R.; Griessen, R.; Groot, D. G. d. *J. Phys. F: Met. Phys.* **1986**, *16*, 1933−1952.

(85) Schirber, J. E.; Morosin, B. *Phys. Rev. B* **1975**, *12*, 117−118.

(86) Yevick, A.; Frenkel, A. I. *Phys. Rev. B* **2010**, *81*, 115451.

(87) Land, T. A.; Michely, T.; Behm, R. J.; Hemminger, J. C.; Comsa, G. *Surf. Sci.* **1992**, *264*, 261−270.

(88) Lytle, F. W.; Greegor, R. B.; Marques, E. C.; Sandstrom, D. R.; Via, G. H.; Sinfelt, J. H. *J. Catal.* **1985**, *95*, 546−557.

(89) Kang, J. H.; Menard, L. D.; Nuzzo, R. G.; Frenkel, A. I. *J. Am. Chem. Soc.* **2006**, *128*, 12068−12069.

(90) Ditlevsen, P. D.; Van Hove, M. A.; Somorjai, G. A. *Surf. Sci.* **1993**, *292*, 267−275.

(91) Kua, J.; Goddard, W. A. *J. Phys. Chem. B* **1998**, *102*, 9492−9500.

(92) Watwe, R. M.; Cortright, R. D.; Nørskov, J. K.; Dumesic, J. A. *J. Phys. Chem. B* **2000**, *104*, 2299−2310.

(93) Vaarkamp, M.; Miller, J. T.; Modica, F. S.; Koningsberger, D. C. *J. Catal.* **1996**, *163*, 294−305.

(94) Fan, C. Z.; Sun, L. L.; Wang, Y. X.; Liu, R. P.; Zeng, S. Y.; Wang, W. K. *Physica B* **2006**, *381*, 174−178.

(95) Mankad, V.; Rathod, N.; Gupta, S. D.; Gupta, S. K.; Jha, P. K. *Mater. Chem. Phys.* **2011**, *129*, 816−822.

(96) Dent, A. J.; Evans, J.; Fiddy, S. G.; Jyoti, B.; Newton, M. A.; Tromp, M. *Angew. Chem., Int. Ed.* **2007**, *46*, 5356−5358.

(97) Singh, J.; Alayon, E. M. C.; Tromp, M.; Safonova, O. V.; Glatzel, P.; Nachtegaal, M.; Frahm, R.; Bokhoven, J. A. v. *Angew. Chem., Int. Ed.* **2008**, *47*, 9260−9264.

(98) Grunwaldt, J.-D.; Kimmerle, B.; Baiker, A.; Boye, P.; Schroer, C. G.; Glatzel, P.; Borca, C. N.; Beckmann, F. *Catal. Today* **2009**, *145*, 267−278.

(99) Merte, L. R.; Behafarid, F.; Miller, D. J.; Friebel, D.; Cho, S.; Mbuga, F.; Sokaras, D.; Alonso-Mori, R.; Weng, T.-C.; Nordlund, D.; Nilsson, A.; Roldan Cuenya, B. *ACS Catal.* **2012**, *2*, 2371−2376.

(100) Frenkel, A. I.; Cason, M. W.; Elsen, A.; Jung, U.; Small, M. W.; Nuzzo, R. G.; Vila, F. D.; Rehr, J. J.; Stach, E. A.; Yang, J. C. *J. Vac. Sci. Technol., A* **2014**, *32* (020801), 1−17.

(101) Frenkel, A. I.; Bokhoven, J. A. v. *J. Synchrotron Radiat.* **2014**, *21*, 1084−1089.

(102) Frenkel, A. I. *Chem. Soc. Rev.* **2012**, *41*, 8163−8178.

(103) Frenkel, A. I.; Wang, Q.; Sanchez, S. I.; Small, M. W.; Nuzzo, R. G. *J. Chem. Phys.* **2013**, *138*, 064202.

(104) Hämäläinen, K.; Siddons, D. P.; Hastings, J. B.; Berman, L. E. *Phys. Rev. Lett.* **1991**, *67*, 2850−2853.

(105) Safonova, O. V.; Tromp, M.; Bokhoven, J. A. v.; de Groot, F. M. F.; Evans, J.; Glatzel, P. *J. Phys. Chem. B* **2006**, *110*, 16162−16164.

(106) Pushkar, Y.; Yano, J.; Glatzel, P.; Messinger, J.; Lewis, A.; Sauer, K.; Bergmann, U.; Yachandra, V. *J. Biol. Chem.* **2007**, *282*, 7198−7208.

(107) Yano, J.; Pushkar, Y.; Glatzel, P.; Lewis, A.; Sauer, K.; Messinger, J.; Bergmann, U.; Yachandra, V. *J. Am. Chem. Soc.* **2005**, *127*, 14974−14975.

(108) Glatzel, P.; Singh, J.; Kvashnina, K. O.; Bokhoven, J. A. v. *J. Am. Chem. Soc.* **2010**, *132*, 2555−2557.

(109) Yano, J.; Kern, J.; Pushkar, Y.; Sauer, K.; Glatzel, P.; Bergmann, U.; Messinger, J.; Zouni, A.; Yachandra, V. K. *Philos. Trans. R. Soc., B* **2008**, *363*, 1139−1147.

(110) Frenkel, A. I.; Small, M. W.; Smith, J. G.; Nuzzo, R. G.; Kvashnina, K. O.; Tromp, M. *J. Phys. Chem. C* **2013**, *117*, 23286−23294.

(111) Bordiga, S.; Groppo, E.; Agostini, G.; Bokhoven, J. A. v.; Lamberti, C. *Chem. Rev.* **2013**, *113*, 1736−1850.